SLAC-PUB-16126

Angular dependence of betatron x-ray spectra from a laser wakefield accelerator

F. Albert[1*], B. B. Pollock[1], J. L. Shaw[2], K. A. Marsh[2], J. E. Ralph[1], Y.-H. Chen[1], D. Alessi[1], A. Pak[1], C. E. Clayton[2], S. H. Glenzer[3] and C. Joshi[2]

[1] *Lawrence Livermore National Laboratory, NIF and Photon Sciences, 7000 East Avenue, Livermore CA 94550, USA*

[2] *Department of Electrical Engineering, University of California, Los Angeles CA 90095, USA*

[3] *SLAC National Accelerator Laboratory, Stanford CA 94309, USA*

(Dated: August 6, 2013)

We present the first measurements of the angular dependence of the betatron x-ray spectrum, produced by electrons inside the cavity of a laser-wakefield accelerator. Electrons accelerated up to 300 MeV energies produce a beam of broadband, forward-directed betatron x-ray radiation extending up to 80 keV. The angular resolved spectrum from an image plate-based spectrometer with differential filtering provides data in a single laser shot. The simultaneous spectral and spatial x-ray analysis allows for a 3D reconstruction of electron trajectories with a micrometer resolution, and we find that the angular dependence of the x-ray spectrum is showing strong evidence of anisotropic electron trajectories.

The development of efficient x-ray probes with energies larger than 10 kiloelectronvolts (keV) has become essential for High Energy Density (HED) science experiments. These experiments produce highly transient matter under extreme states of temperatures and pressures. For instance, high energy x-rays are used to radiograph the dynamics of imploding capsules at the National Ignition Facility (NIF) [1], or the temperature and pressure of warm dense matter via absorption spectroscopy [2] or scattering [3, 4] techniques. Betatron x-ray radiation, produced when relativistic electrons oscillate in a beam-driven [5] or laser-driven [6–8] plasma channel, is an x-ray source holding great promise for future HED experiments. X-rays produced in this manner are ultrashort, directional, spatially coherent, and broadband, making them highly attractive as a probe.

Betatron x-ray radiation is readily produced when electrons are accelerated at an ultra-high gradient in a laser-wakefield accelerator (LWFA) [9–12]. In the three dimensional (3D), highly nonlinear LWFA regime, when a short but highly intense laser pulse with an intensity $I > 10^{18}$ W/cm^{-3} is focused inside a plasma, the laser ponderomotive force completely expels the plasma electrons away from the strong intensity regions to form an ion bubble in the wake of the pulse [13]. Electrons trapped at the back of this structure are accelerated and wiggled by the focusing force of the more massive and thus immobile ions to produce broadband, synchrotron-like radiation in the keV energy range [14, 15]. Previous work has implied that the betatron x-rays have a source size of a few microns [8, 16], a divergence of less than 100 mrad [17], and a pulse duration of less than 100 fs [18]. Because betatron x-rays are directly related to the electrons emitting them, the radiative properties of the source are also an excellent diagnostic of the acceleration process in a LWFA. The electron beam emittance and size can be inferred from the x-ray beam profile [17, 19], spectrum [20, 21], or source size [22], using various x-ray spectroscopy and imaging techniques. In these experiments, however, typical betatron x-ray spectral diagnostics such as filters, crystal spectrometers, single-shot counting mode CCDs, or other semi-conductors do not provide single-shot simultaneous spectral and spatial resolution of the radiation.

We show in this Letter that the angular dependence of the betatron spectrum is well explained by the anisotropy of the electron trajectories. In particular, we tomographically reconstruct the trajectories of the electrons that emit these x-rays inside the laser-produced wake from a single-shot angular measurement of the betatron x-ray spectrum and the beam profile at different energies. This measurement, performed by means of a stacked image-plate spectrometer with differential filtering, has enabled us to observe betatron x-rays with energies extending up to 80 keV. The resulting 3D reconstruction of the accelerating electron trajectories inside the LWFA explains the measured angular distribution of the betatron x-ray spectrum, which is important for betatron x-rays imaging or spectroscopy experiments.

In a LWFA, the motion of an electron accelerated along $\vec{u_z}$ with momentum $\vec{p}$ and position $\vec{r}$ in the wake of a laser pulse can be described by the Lorentz equation of motion:

$$\frac{d\vec{p}}{dt} = -m\omega_p^2 \frac{\vec{r}}{2} + \alpha \frac{mc\omega_p}{e}\vec{u_z}, \tag{1}$$

where m is the electron rest mass, e is the elementary charge, and $\omega_p = \sqrt{n_e e^2/m\epsilon_0}$ is the plasma frequency. Here, n_e is the electron density, ϵ_0 is the vacuum permittivity and c is the vacuum speed of light. In the blowout 3D nonlinear regime of laser wakefield acceleration [13], $\alpha = \frac{1}{2}\sqrt{a_0}$ is the normalized accelerating field, where $a_0 = 8.5\times10^{-10}\lambda_0[\mu\text{m}]\, I^{1/2}[\text{W/cm}^2]$ is the laser normalized vector potential. The electron trajectory is used to calculate the intensity I radiated by the particle per unit frequency ω and solid angle Ω [23]:

$$\frac{d^2I}{d\Omega d\omega} = \frac{e^2\omega^2}{4\pi c}\left|\int_{-\infty}^{\infty} \vec{n}\times\left(\vec{n}\times\vec{\beta}\right) e^{i\omega(t-\frac{\vec{n}.\vec{r}}{c})}dt\right|^2, \tag{2}$$

This material is based upon work supported by the U.S. Department of Energy, Office of Science, Office of Basic Energy Sciences, under Contract No. DE-AC02-76SF00515.

where $\vec{n}$ is the vector corresponding to the direction of observation and $\beta = v/c$ the normalized electron velocity. In the case where the wiggler parameter $K = 1.33 \times 10^{-10}\sqrt{\gamma n_e} r$ is larger than unity, the spectrum, observed at an angle θ from the plane in which the particle oscillates, can be approximated by the asymptotic limit [23, 24]:

$$\frac{d^2I}{d\Omega d\omega} = \frac{e^2}{3\pi^2 c}\left(\frac{\omega\rho}{c}\right)^2\left(\frac{1}{\gamma^2}+\theta^2\right) \times \left[K_{2/3}^2(\xi) + \frac{\theta^2}{(1/\gamma^2)+\theta^2}K_{1/3}^2(\xi)\right], \quad (3)$$

where $K_{2/3}$ and $K_{1/3}$ are modified Bessel functions. Here, ρ is the radius of curvature of the electron trajectory and $\xi = \frac{\omega\rho}{3c}\left(\frac{1}{\gamma^2}+\theta^2\right)^{3/2}$. Hence, for $\theta = 0$, the x-ray spectrum peaks at $\omega \sim 0.45\omega_c$, where $\hbar\omega_c$[keV]$=5\times 10^{-24}\times\gamma^2 n_e$[cm^{-3}]$r$[$\mu$m] is the critical energy. The peak x-ray energy also decreases with the observation angle and in this paper we present the first experimental measurement of the angular dependence of the betatron x-ray spectrum.

The experiment was conducted at the Jupiter Laser Facility, Lawrence Livermore National Laboratory, using the Callisto laser system. Callisto is a 200 TW laser delivering pulses of 60 fs (full width at half maximum, fwhm) duration with energies up to 12 J at a repetition rate of 1 shot/30 min. The experimental setup is shown in Fig. 1. Using an f/8 off-axis parabola, we focused the laser onto the edge of a 10-mm-long gas cell, with a 500 μm and 1 mm entrance and exit pinhole, respectively. The focal spot, measured at low laser power, is 12 μm (fwhm), and $a_0 \sim 2$. The background electron density of the plasma is measured with interferometry by using a 100 fs probe pulse synchronized with the main laser pulse. The density of the plasma is reconstructed by Abel inverting the measured phase shift imparted by the plasma to the probe beam [25]. The electron beam properties are measured with a two-screen electron spectrometer [26–28]. As shown in Fig. 1, the electrons are vertically deflected by a 0.42 Tesla, 21-cm-long permanent dipole magnet onto two image plates (model FUJI-MS-2040), respectively IP$_a$ and IP$_b$ to calculate the energy and deflection of the electron beam. The betatron x-rays propagate outside of the vacuum target chamber through a 65 μm mylar window and a 50 μm Al filter to block any residual laser light. The betatron beam profile is measured on IP$_a$, and after transmission through IP$_a$, the x-ray beam propagates through a series of image plates alternatively stacked with filters of increasing Z number. The final filters are lead sheets with increasing thicknesses (1-4 mm) [29]. This diagnostic can detect and spectrally resolve broadband x-ray radiation up to 1 MeV through 15 successive channels, with an acceptance angle of 40 mrad. Fig. 1 also shows the spectrometer data in channels 1-6.

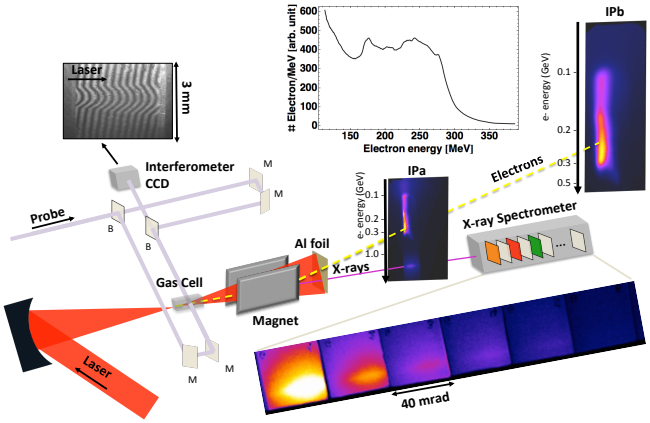

FIG. 1. Schematic of the experimental setup, showing the f/8 off-axis parabola focusing the laser pulse on the gas cell target, and the transverse interferometry probe. The interferometer has two beam splitters (B) and four mirrors (M). An example of an interferogram is shown above the interferometer CCD camera. The electrons (dashed line) are dispersed in energy by the magnet centered on the laser axis and located 3.5 cm from the source inside the target chamber and then recorded on image plates (IP$_a$ and IP$_b$, located 37.2 cm and 111.1 cm away from the magnet exit, respectively). The corresponding retrieved electron beam spectrum is shown on top. After exiting the vacuum chamber, x-rays (solid line) propagate through 7.3 cm of air and through IP$_a$ onto the 15 channel x-ray spectrometer, below which are shown raw images (25 μm pixels) from channels 1-6.

Fig. 2 shows the on-axis x-ray energy deposited in each channel (within a circle diameter of 30 pixels/ 1 mrad). The laser parameters for this shot are $E = 5.3$ J and $a_0 = 2.33$, with a gas cell filled with 100 % He at $n_e = 6 \times 10^{18}$ cm^{-3}. We observe a broadband electron spectrum with a maximum energy of 268±25 MeV and spectral features, as well as shot-to-shot fluctuations sensitive to both laser and plasma parameters. The x-ray data shown in Fig. 2 are fitted with Eq. 3. On axis ($\theta = 0$), the betatron critical energy $\hbar\omega_c$ is $\simeq 17.5 \pm 2.5$ keV, with the x-ray spectrum peaking at 7.9±1.1 keV, and a tail extending up to 80 keV. Also shown in Fig. 2 is the spectral response of channels 1-6 of the spectrometer to a synchrotron spectrum with a 20 keV critical energy. In addition to synchrotron spectra with different critical energies, the data of Fig. 2 is fitted with a numerically-calculated spectrum emitted by an electron with a certain initial displacement from the axis and accelerated by a wakefield of constant amplitude $eE/m\omega_p c = 0.763$. The spectrum is calculated by first solving Eq. 1 with a 4th order Runge-Kutta algorithm to calculate the electron trajectories in the plasma. The full on-axis x-ray spectrum is calculated by integrating the x-ray spectra (Eq. 3) along the whole trajectory using 1500 time steps (with each step $dt = 0.4c/\omega_p$), and 100 eV energy increments. Because the final electron energy and the background

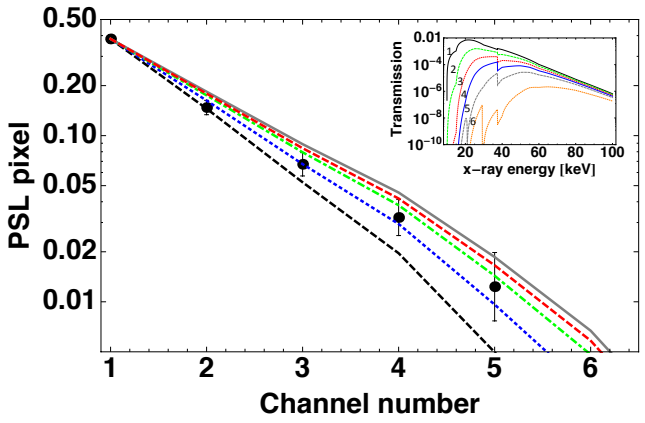

FIG. 2. X-ray spectrometer signal, in channels 1-6 (photostimulated luminescence, PSL, per pixel) with theoretical fits, corresponding to the spectrometer response to a betatron spectrum with a critical energy of 10 keV, 15 keV, 20 keV and 25 keV (dashed, dotted, dot-dashed and solid line, respectively) and to the radiation produced by an electron injected 5 μm off-axis and accelerated up to 268 MeV (red dashed line). The inset shows the spectral response of each spectrometer channel (labeled 1-6) to a synchrotron spectrum with a critical energy of 20 keV.

density are measured during the experiment, the remaining free parameter to adjust is the radius of injection r_0, and in this case, we use $r_0 = 5$ μm. Other input parameters in the calculation, such as the initial electron energy and the normalized accelerating field, are calculated using an analytical model that describes the fields and accelerated electron energies created in the 3D nonlinear blowout regime [13]. For the data presented in Fig. 2, we have $\alpha = 0.763$ and $\gamma_i = \gamma_\Phi = \omega_0/\sqrt{3}\omega_p = 9.85$. The analytic fits to the observed spectrum shown in Fig. 2 indicate the measured spectrum contains contributions from electrons radiating over a range of critical energies from 15-20 keV. This range in critical energies is to be expected for electrons that oscillate over a range of radii. Using the relationship $\hbar\omega_c[\mathrm{keV}]=5\times10^{-24}\times\gamma^2 n_e[\mathrm{cm}^{-3}]r[\mu\mathrm{m}]$, we can estimate the range in r_0 to be 5 ± 0.7 μm. The injection radius r_0 damps from 5 μm to $r_f \sim 2$ μm when γ increases to 520. Since the critical energy scales with γ^2, most of the measured hard x-rays are produced by electrons toward the end of their trajectories. A source size with radius $r = 2$ μm is consistent with previous measurements [16, 17, 22].

To retrieve the spatial orientation of the electron trajectories, Eq. 2 is used to self consistently match the observed spatial and spectral profiles of the experimentally measured betatron beam profile. The experimental beam profile recorded on IP$_a$ is shown in Fig. 3 (a). The response function of the image plates to x-rays in the energy range 5-100 keV has been calibrated [30], and for our experimental configuration, the response peaks at 15 keV. The shape displayed by this beam profile is not completely elliptical as one would expect from a single electron oscillating about the axis [17]. To reproduce this profile using a single particle trajectory tracking method, we use Eq. 2 to map the full spatial and spectral distribution of the betatron radiation. Fig. 3 (a) also shows the theoretical x-ray beam profile, convolved with the response function of IP$_a$. This beam profile is obtained by distributing particles and injecting them in a plane (x, y) perpendicular to the direction of electron acceleration z. The particles are distributed on a circle of radius $r_0 = 5$ μm in the (x, y) plane with angular steps of $\pi/30$ over an angular distribution. In Fig 3 (b) we show this angular distribution of electrons as a function of angle, and for four groups of electrons with different final energies representative of the overall spectrum displayed in Fig. 1 (with extrapolation for the lower electron energies). The corresponding final relativistic factors are: $\gamma_f = 520$, $\gamma_f = 440$, $\gamma_f = 200$, and $\gamma_f = 100$. This range of energies is due to the fact that the electron spectrum is not monoenergetic and that electrons were injected into the wake at different times. In this figure, the laser polarization corresponds to $\theta = \pi/2$ (linear, horizontal polarization). The resulting 3D reconstruction of electron trajectories in the plasma is shown in Fig. 3 (c), for the same four groups of electrons. For each trajectory, the dephasing length is L_{dp}=0.29 cm, and electrons injected later into the wake end with a lower final energy. This reconstruction is specific to our model. We have assumed complete blowout and electrons trapped in the first bucket of the wake, as well as no anisotropy and coupling in the radial focussing forces. Several factors can explain the anisotropy observed on the electron distribution. In our case, the high-energy particles oscillate primarily along the laser polarization direction, while the lower energy particles of the electron spectrum tend to have a more isotropic distribution along the propagation axis. This observation could indicate strong interaction between the electron beam and the back of the laser pulse at the end of the acceleration, as reported in previous papers [31]. At $n_e = 6\times10^{18}$ cm^{-3} and for a coupled laser power P = 44 TW (50% coupling efficiency), the dephasing length $L_{dp}[\mathrm{cm}]\simeq (P[\mathrm{TW}])^{1/6}(10^{18}[\mathrm{cm}^{-3}]/n_e)^{4/3} \simeq 0.2^{+0.13}_{-0.04}$ cm is shorter than the length of the gas cell, and the most energetic electrons may interact with the back of the laser pulse to oscillate primarily in the direction of laser polarization. However, other effects, such as pulse front tilt [32], have been shown to strongly influence the direction of the electron oscillations.

We finally find that the angular dependance of the betatron x-ray spectrum is perfectly explained by the above tomographic reconstruction of electron trajectories. Fig 4 shows the variation of the peak x-ray energy with the observation angle. The data of Fig. 4 are fitted with three different theoretical spectra obtained from: the synchrotron radiation formula with $\omega_c = 20$ keV, the

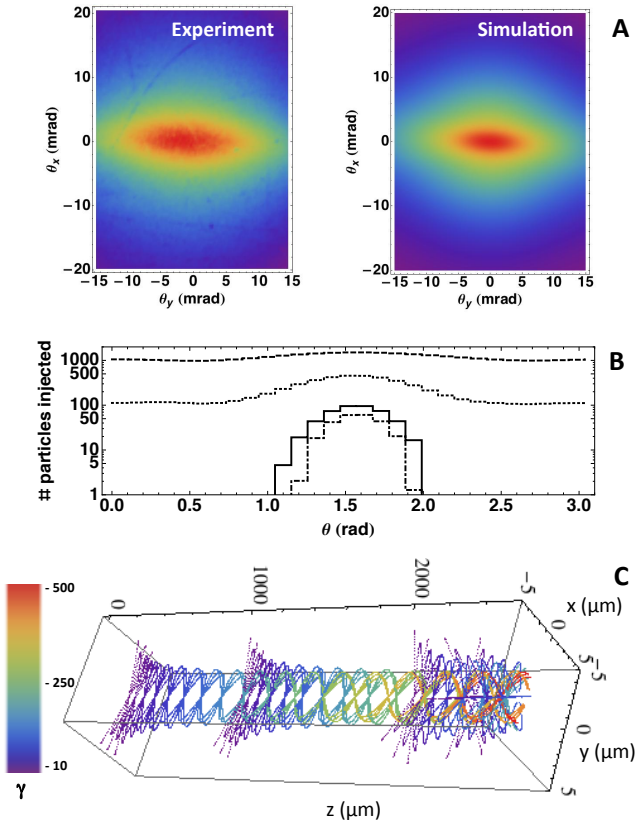

FIG. 3. (A) Experimentally measured and calculated betatron x-ray beam profile, recorded on IP_a, scanned with a 200 μm pixel size. The electron distribution around the propagation axis (positive z direction) is shown in (B) for four distinct groups of electrons accelerated up to $\gamma_f = 100$, 200, 440, and 520 (dashed, dotted, solid, and dot-dashed lines, respectively). $\theta = \pi/2$ rad corresponds to the laser polarization direction. (C) Sample trajectories showing the three dimensional motion of the four groups electrons in the plasma, from trapping up to their final energies.

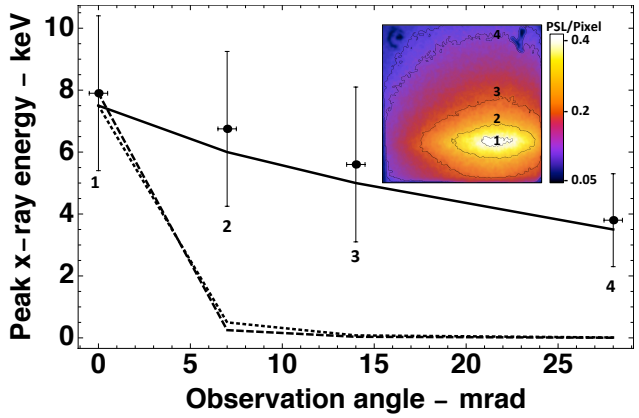

FIG. 4. Peak experimental betatron x-ray energy as a function of the angle of observation (dots with error bars). The spectrum was measured on axis and at 7 mrad, 14 mrad and 28 mrad corresponding to respective vertical positions 1, 2, 3, 4 indicated in the inset showing the beam profile on the first spectrometer channel. The three curves show the theoretical peak energy for Eq. 3 (dashed line), a single electron oscillating in the plasma (dotted line) and the full set of electron trajectories (solid line).

radiation emitted by a single electron wiggled and accelerated by the plasma, and the full radiation emitted by the multiple trajectories of Fig. 3 (c). The first two cases do not reproduce the experimental angular dependence of the x-ray spectrum because they assume that electrons oscillate along only one direction. Although the most energetic particles primarily oscillate along the laser polarization axis, a larger number of lower-energy electrons oscillate with a wider range of angles in the transverse plan. This results in a softer decrease of the peak x-ray energy with increasing observation angles, a first experimental observation that only multiple, 3D trajectories can reproduce.

In conclusion, we have reconstructed the injection radius and the orientation of the accelerating electron beam in a LWFA from the simultaneously observed spatial and spectral distribution of the betatron x-rays in a single shot. The asymmetry in the betatron image was found to be consistent with the anisotropy of the angular distribution and the energy of the electrons. In the future this tomographic reconstruction technique can be further improved to take into account the angular spread, injection phase and a spread in the injection radius, thereby making the betatron radiation a powerful self-probe of the LWFA in addition to being a probe for future HED science experiments. Understanding the origin of and measuring the angular dependance of the betatron x-ray spectrum is important for near-term single-shot HED experiments using pump-probe, scattering, imaging and spectroscopic techniques.

This work was performed under the auspices of the U.S. Department of Energy under contract DE-AC52-07NA27344 at LLNL, DE-FG02-92-ER40727 at UCLA, and supported by the Laboratory Directed Research and Development (LDRD) Program under tracking code 13-LW-076. The authors thank R.C. Cauble, J. Bonlie and S. Maricle for their support of the Callisto laser system at the Jupiter Laser Facility, and C. Haefner for advice on lasers. F. A. acknowledges discussions with F. V. Hartemann on theory and modeling and thanks C. D. Chen for discussions on the spectrometer layout.

[1] D. Hicks and et al, Phys. Plasmas **19**, 122702 (2012).

[2] A. Benuzzi-Mounaix, F. Dorchies, V. Recoules, F. Festa, O. Peyrusse, A. Levy, A. Ravasio, T. Hall, M. Koenig, N. Amadou, E. Bambrink, and S. Mazevet, Phys. Rev. Lett. **107**, 165006 (2011).

[3] A. L. Kritcher, P. Neumayer, J. Castor, T. Doppner, R. W. Falcone, O. L. Landen, H. J. Lee, R. W. Lee, E. C. Morse, A. Ng, S. Pollaine, D. Price, and S. H. Glenzer, Science **322**, 69 (2008).

[4] S. H. Glenzer and R. Redmer, Rev. Mod. Phys **81**, 1625 (2009).

[5] S. Wang, C. E. Clayton, B. E. Blue, E. S. Dodd, K. A. Marsh, W. B. Mori, C. Joshi, S. Lee, P. Muggli, T. Katsouleas, F. J. Decker, M. J. Hogan, R. H. Iverson, P. Raimondi, D. Walz, R. Siemann, and R. Assmann, Phys. Rev. Lett. **88**, 135004 (2002).

[6] A. Rousse, K. T. Phuoc, R. Shah, A. Pukhov, E. Lefebvre, V. Malka, S. Kiselev, F. Burgy, J.-P. Rousseau, D. Umstadter, and D. Hulin, Phys. Rev. Lett. **93**, 135005 (2004).

[7] S. Corde, K. T. Phuoc, G. Lambert, R. Fitour, V. Malka, and A. Rousse, Rev. Mod. Phys. **85**, 1 (2013).

[8] S. Kneip, C. McGuffey, J. L. Martins, S. F. Martins, C. Bellei, V. Chvykov, F. Dollar, R. Fonseca, C. Huntington, G. Kalintchenko, A. Maksimchuk, S. P. D. Mangles, T. Matsuoka, S. R. Nagel, C. A. J. Palmer, J. Schreiber, K. T. Phuoc, A. G. R. Thomas, V. Yanovsky, L. O. Silva, K. Krushelnick, and Z. Najmudin, Nat. Phys. **6**, 980 (2010).

[9] T. Tajima and J. M. Dawson, Phys. Rev. Lett. **43**, 267 (1979).

[10] S. P. D. Mangles, C. D. Murphy, Z. Najmudin, A. G. R. Thomas, J. L. Collier, A. E. Dangor, E. J. Divall, P. S. Foster, J. G. Gallacher, C. J. Hooker, D. A. Jaroszynski, A. J. Langley, W. B. Mori, P. A. Norreys, F. S. Tsung, R. Viskup, B. R. Walton, and K. Krushelnick, Nature **431**, 535 (2004).

[11] C. G. R. Geddes, C. Toth, J. V. Tilborg, E. Esarey, C. B. Schroeder, D. Bruhwiler, C. Nieter, J. Cary, and W. P. Leemans, Nature **431**, 538 (2004).

[12] J. Faure, Y. Glinec, A. Pukhov, S. Kiselev, S. Gordienko, E. Lefebvre, J.-P. Rousseau, F. Burgy, and V. Malka, Nature **431**, 541 (2004).

[13] W. Lu, M. Tzoufras, C. Joshi, F. S. Tsung, W. B. Mori, J. Vieira, R. A. Fonseca, and L. O. Silva, Phys. Rev. ST Acc. Beams **10**, 061301 (2007).

[14] F. Albert, R. Shah, K. T. Phuoc, R. Fitour, F. Burgy, J.-P. Rousseau, A. Tafzi, D. Douillet, T. Lefrou, , and A. Rousse, Phys. Rev. E. **77**, 056402 (2008).

[15] S. Fourmaux, S. Corde, K. T. Phuoc, P. M. Leguay, S. Payeur, P. Lassonde, S. Gnedyuk, G. Lebrun, C. Fourment, V. Malka, S. Sebban, A. Rousse, and J. C. Kieffer, New J. Phys. **13**, 033017 (2011).

[16] R. C. Shah, F. Albert, K. T. Phuoc, O. Shevchenko, D. Boschetto, A. Pukhov, S. Kiselev, F. Burgy, J.-P. Rousseau, and A. Rousse, Phys. Rev. E **74**, 045401(R) (2006).

[17] K. T. Phuoc, S. Corde, R. Shah, F. Albert, R. Fitour, J.-P. Rousseau, F. Burgy, B. Mercier, and A. Rousse, Phys. Rev, Lett **97**, 225002 (2006).

[18] K. T. Phuoc, R. Fitour, A. Tafzi, T. Garl, N. Artemiev, R. Shah, F. Albert, D. Boschetto, A. Rousse, D.-E. Kim, A. Pukhov, V. Seredov, and I. Kostyukov, Phys. Plasmas **14**, 080701 (2007).

[19] S. Corde, C. Thaury, A. Lifschitz, G. Lambert, K. T. Phuoc, X. Davoine, R. Lehe, D. Douillet, A. Rousse, and V. Malka, Nat. Comm. **4**, 1501 (2013).

[20] G. R. Plateau, C. G. R. Geddes, D. B. Thorn, M. Chen, C. Benedetti, E. Esarey, A. J. Gonsalves, N. H. Matlis, K. Nakamura, C. B. Schroeder, S. Shiraishi, T. Sokollik, J. V. Tilborg, C. Toth, S. Trotsenko, T. S. Kim, M. Battaglia, T. Stohlker, and W. P. Leemans, Phys. Rev. Lett. **109**, 064802 (2012).

[21] M. Schnell, A. Savert, B. Landgraf, M. Reuter, M. Nicolai, O. Jackel, C. Peth, T. Thiele, O. Jansen, A. Pukhov, O. Willi, M. C. Kaluza, and C. Spielmann., Phys. Rev. Lett. **108**, 075001 (2012).

[22] S. Kneip, C. McGuffey, J. L. Martins, M. S. Bloom, V. Chvykov, F. Dollar, R. Fonseca, S. Jolly, G. Kalintchenko, K. Krushelnick, A. Maksimchuk, S. P. D. Mangles, Z. Najmudin, C. A. J. Palmer, K. T. Phuoc, W. Schumaker, L. O. Silva, J. Vieira, V. Yanovsky, and A. G. R. Thomas, Phys. Rev. ST Accel. Beams **15**, 021302 (2012).

[23] J. Jackson, *Classical Electrodynamics*, edited by J. Wiley and N. Y. Sons (1998).

[24] E. Esarey, B. A. Shadwick, P. Catravas, and W. P. Leemans, Phys. Rev. E **65**, 056505 (2002).

[25] J. Shaw, *Characterization of sub-millimeter scale gas cells as possible injectors for staged laser wakefield acceleration*, Master's project, University of California Los Angeles (2013).

[26] I. Blumenfeld, C. E. Clayton, F.-J. Decker, M. J. Hogan, C. Huang, R. Ischebeck, R. Iverson, C. Joshi, T. Katsouleas, N. Kirby, W. Lu, K. A. Marsh, W. B. Mori, P. Muggli, E. Oz, R. H. Siemann, D. Walz, and M. Zhou, Nature **445**, 741 (2006).

[27] C. E. Clayton, J. E. Ralph, F. Albert, R. A. Fonseca, S. H. Glenzer, C. Joshi, W. Lu, K. A. Marsh, S. F. Martins, W. B. Mori, A. Pak, F. S. Tsung, B. B. Pollock, J. S. Ross, L. O. Silva, and D. H. Froula, Phys. Rev. Lett **105**, 105003 (2010).

[28] B. B. Pollock, C. E. Clayton, J. E. Ralph, F. Albert, A. Davidson, L. Divol, C. Filip, S. H. Glenzer, K. Herpoldt, W. Lu, K. A. Marsh, J. Meinecke, W. B. Mori, A. Pak, T. C. Rensink, J. S. Ross, J. Shaw, G. R. Tynan, C. Joshi, and D. H. Froula, Phys. Rev. Lett **107**, 045001 (2011).

[29] C. D. Chen, J. A. King, M. H. Key, K. U. Akli, F. N. Beg, H. Chen, R. R. Freeman, A. Link, A. J. Mackinnon, A. G. MacPhee, P. K. Patel, M. Porkolab, R. B. Stephens, and L. D. V. Woerkom, Rev. Sc. Instr. **79**, 10E305 (2008).

[30] B. R. Maddox, H. S. Park, B. A. Remington, N. Izumi, S. Chen, C. Chen, G. Kimminau, Z. Ali, M. J. Haugh, and Q. Ma, Rev. Sc. Instr. **82**, 023111 (2011).

[31] S. P. D. Mangles, A. G. R. Thomas, M. C. Kaluza,

O. Lundh, F. Lindau, A. Persson, F. S. Tsung, Z. Najmudin, W. B. Mori, C.-G. Wahlstrm, and K. Krushelnick, Phys. Rev. Lett. **96**, 215001 (2006).
[32] A. Popp, J. Vieira, J. Osterhoff, Z. Major, R. Hrlein, M. Fuchs, R. Weingartner, T. P. Rowlands-Rees, M. Marti, R. A. Fonseca, S. F. Martins, L. O. Silva, S. M. Hooker, F. Krausz, F. Grner, , and S. Karsch, Phys. Rev. Lett. **105**, 215001 (2010).